Chapter 8
In Situ and Ex Situ Spectrophotometric Characterization of Single- and Multilayer-Coatings II: Experimental Technique and Application Examples

Steffen Wilbrandt and Olaf Stenzel

Abstract In the previous chapter, the theoretical background for characterization of single layer and multilayer coatings has been outlined. In this chapter, important aspects for the underlying experimental techniques will presented. Furthermore, we demonstrate the application of different dispersion models for characterization of uncoated substrates, single layer coatings of dielectrics, semiconductors, metals and organic coatings. Thereby, the focus has been set to the β_do model. Finally, the interplay of in situ and ex situ spectroscopy will be demonstrated for a multilayer antireflection coating (V-coating).

8.1 Experimental Techniques in Spectrophotometry

Let us for a moment return to Fig. 1.1. Imagine the very simplest case—a monochromatic plane light wave that is incident onto the sample with a light intensity I_E. In a complex notation, the electric field E of that light wave depends on the time t and the coordinates r according to (2.1).

S. Wilbrandt (✉)
Fraunhofer Institute for Applied Optics and Precision Engineering IOF, Albert-Einstein-Str. 7, 07745 Jena, Germany
e-mail: steffen.wilbrandt@iof.fraunhofer.de

O. Stenzel
Fraunhofer Institute for Applied Optics and Precision Engineering IOF, Albert-Einstein-Str. 7, 07745 Jena, Germany
e-mail: olaf.stenzel@iof.fraunhofer.de; optikbuch@optimon.de

O. Stenzel
Abbe School of Photonics, Friedrich-Schiller-University Jena, Albert-Einstein-Straße 6, 07745 Jena, Germany

O. Stenzel and M. Ohlídal (eds.), *Optical Characterization of Thin Solid Films*, Springer Series in Surface Sciences 64,
https://doi.org/10.1007/978-3-319-75325-6_8

Once our focus is on spectrophotometry, it is the intensity of the light that has to be discussed in more detail. It is given by (2.2). In ex situ coating characterization practice, the experimental determination of T_{exp} and R_{exp} as defined in (2.3) is usually performed by means of commercial spectrophotometers, which may be roughly divided into dispersive and Fourier transform spectrophotometers [1]. Let us mention in this context, that for coating characterization purposes, highest absolute accuracy in intensity measurements is utmost important for getting reliable results from minimizing discrepancy functions like (7.15) while highest spectral resolution is usually not of use. Thereby, T_{calc} and R_{calc} are theoretical spectra, which are calculated within a certain layer model.

8.1.1 Spectral Resolution

A usual and convenient assumption in the applied layer model is, that the film is thin enough for observing interference phenomena that arise from multiple internal reflections in the film. On the other hand, the substrate should be thick enough so that multiple internal reflections within the substrate superimpose incoherently, e.g. without observable interference. This defines a constraint to the allowed spectral resolution in the corresponding measurement: A too high resolution would resolve interference effects in the substrate, which is no more consistent with the assumed incoherent superposition of internally reflected light trains within the thick substrate. As a rough estimate, the spectral resolution in the T- and R-measurements at near normal incidence should therefore be restricted so that (8.1) is fulfilled [2]:

$$\Delta\nu > \frac{1}{2\pi n_{sub} h_{sub}} \text{ or } \Delta\lambda > \frac{\lambda^2}{2\pi n_{sub} h_{sub}} \tag{8.1}$$

Here, $\Delta\nu$ or $\Delta\lambda$ denote the spectral bandwidth of the incident light (the absolutely monochromatic wave as assumed in (2.2) is only a convenient model assumption, which is never observed in reality in a strong sense). Condition (8.1) is easily fulfilled in characterization practice, because commercial spectrophotometers usually allow setting the spectral bandwidth to a sufficiently large value; or a suitably thick substrate has to be chosen.

On the other hand, highest accuracy in intensity measurements is not so easily achieved. Fortunately, stochastic measurement errors in T or R are not so crucial when performing curve fit s by minimizing (7.15) [3]. The bad news is that systematic measurement errors are highly disturbing [3].

A common source for systematic measurement errors is the limited spectral resolution of the device caused, for example, by the finite width of entrance or exit monochromator slits in a dispersive spectrophotometer. These slits represent rectangular apertures through with light enters into and exits from the monochromator. In an ideal spectrometer, the effect of the finite width of the slit can be modelled in terms of a point spread function with a triangular shape (Fig. 8.1). The obvious result

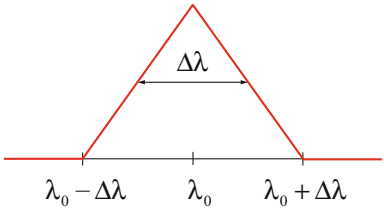

Fig. 8.1 Point spread function of a slit in an ideal spectrometer

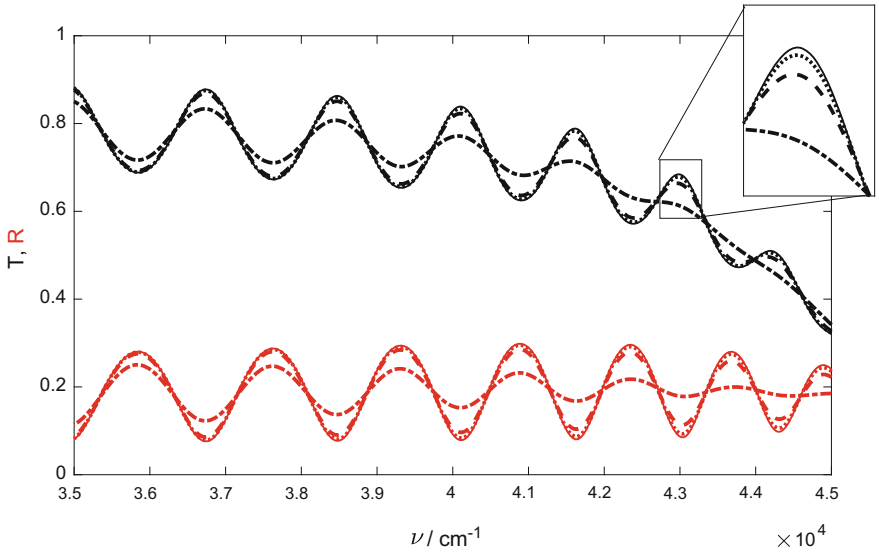

Fig. 8.2 Theoretical transmittance (black) and reflectance (red) assuming a monochromatic wave (solid line) and with effects of a finite spectral bandwidth assuming a triangular point spread function (dotted line: 1 nm, dashed line: 2 nm and dash-dot line: 5 nm slit width)

is a systematic measurement error in transmittance and reflectance, which is largest at the extrema positions of the spectra (Fig. 8.2). The limited spectral resolution of a spectrometer will decrease the measured photometric values at the maxima positions and increase it at the minima position.

In real devices, a more complicated point spread function will be obtained. To take this effect into account, either the point spread function may be included in the calculation of theoretical spectra or a sufficiently high spectral resolution has to be selected during measurement. For an estimation of the required spectral resolution, the impact of the point spread function to a single layer coating can be investigated analytically.

For the special case of vanishing damping, the transmittance at normal incidence of a single layer (refractive index n) on a semi-infinite substrate (refractive index n_{sub}) can be calculated by [2]:

$$T\left(n, n_{sub}, \delta\right) = \frac{n_{sub}\left(\frac{2}{1+n}\right)^2\left(\frac{2n}{n+n_{sub}}\right)^2}{1+\left(\frac{1-n}{1+n}\right)^2\left(\frac{n-n_{sub}}{n+n_{sub}}\right)^2+2\left(\frac{1-n}{1+n}\right)\left(\frac{n-n_{sub}}{n+n_{sub}}\right)cos2\delta} \tag{8.2}$$

with

$$2\delta = 4\pi\nu nh \tag{8.3}$$

It is obvious, that the extrema in transmittance correspond to multiples of π for the 2δ term (weak dispersion presumed). Odd multiplies are quarter-wave (QW) points, even multiplies are half-wave (HW) points.

When applying the triangular point spread function to the transmittance, the expected transmittance $\tilde{T}$ obtained by means of a real spectrometer could be estimated according to:

$$\tilde{T} \approx \frac{1}{4}T\left(n, n_{sub}, \delta - \Delta\delta\right) + \frac{1}{2}T\left(n, n_{sub}, \delta\right) + \frac{1}{4}T\left(n, n_{sub}, \delta + \Delta\delta\right) \tag{8.4}$$

with

$$\Delta\delta = \frac{\pi nh}{\lambda_0^2}\Delta\lambda \tag{8.5}$$

For the measurement errors at the QW- and HW-points, we can deduct:

$$\Delta T_{QW} = T - \tilde{T} \approx -\frac{2n^2 n_{sub}\left(n^2 - n_{sub}^2\right)\left(n^2-1\right)}{\left(n^2+n_{sub}\right)^4}\left(\Delta\delta\right)^2 \tag{8.6}$$

$$\Delta T_{HW} = T - \tilde{T} \approx \frac{2n^2 n_{sub}\left(n^2 - n_{sub}^2\right)\left(n^2-1\right)}{n^4\left(1+n_{sub}\right)^4}\left(\Delta\delta\right)^2 \tag{8.7}$$

From here we see, that the following relations are valid:

$$\left|\Delta T_{QW}\right| < \left|\Delta T_{HW}\right| \text{ for } n > n_{sub} \tag{8.8}$$

$$\left|\Delta T_{QW}\right| > \left|\Delta T_{HW}\right| \text{ for } n < n_{sub} \tag{8.9}$$

In both cases, the largest effect will be observed at the transmittance maxima. For a given accepted tolerance ΔT, the required spectral resolution can be now estimated. For $n > n_{sub}$ we get:

$$\Delta\lambda < \frac{\lambda_0^2\left(1+n_{sub}\right)^2}{\pi h}\sqrt{\frac{\Delta T}{2n_{sub}\left(n^2-n_{sub}^2\right)\left(n^2-1\right)}} \tag{8.10}$$

and for $n < n_{sub}$:

$$\Delta\lambda < \frac{\lambda_0^2 \left(n^2 + n_{sub}\right)^2}{\pi n h} \sqrt{\frac{\Delta T}{2n^2 n_{sub} \left(n^2 - n_{sub}^2\right)\left(n^2 - 1\right)}} \tag{8.11}$$

Together with (8.1), this will confine the spectral resolution suitable for spectrophotometric measurements of the film-on substrate system.

8.1.2 Sample Illumination

Basically, possible illumination configurations can be classified by the relation between the incident light spot and the field of view of the detector (Fig. 8.3 on left). When both areas are identical in shape and size, the reversibility of light enables the use of identical optical configurations for illumination and detection in the case of fiber optic based approaches. This will reduce costs for development, but make this approach sensitive to alignment errors. Even a small misalignment between illumination and detector optics will change the throughput of light and may therefore lead to measurement errors. To overcome this problem, spot sizes for illuminated and collimated light should be different. In principle, either a small spot for the illuminated light and a large spot for collimated light (Fig. 8.3 in center) or vice versa (Fig. 8.3 on right) may be selected. In the case of a small illumination spot, spatial homogeneity of the light source is not required, but is essential for the collimation optic of the detector. Furthermore, in this set-up, any additional light arriving from other sources (ambient light caused by electron beam gun or plasma/ion source) may be problematic. In the opposite case, spatial homogeneity of the light source is crucial, but not required for the collimation optic in front of the detector. In general, spatial homogeneity can be optimized for both cases using diffuser plates, Ulbricht sphere s, light mixing rods, or micro optics arrays.

Diffusing plates and Ulbricht sphere result in significant reduction of the light throughput of the system, while micro optics arrays are expansive. Bearing in mind that unwanted deposition on optics can result in measurement errors, Ulbricht spheres will be advantageous here, because the small port size in relation to the inner surface make it nearly insensitive to unwanted deposition. If the Ulbricht sphere is build up from ceramics, it can withstand high temperatures, and any contaminations can be removed by sandblasting. When the Ulbricht sphere is used as in chamber housing for the light source, it may additionally shield the detector from ambient light.

8.1.3 Transmission and Reflection Measurements

Many commercial spectrophotometers are multiple purpose devices, primarily optimized for performing absorbance measurements in gas or liquid cell geometries. Thin film sample measurements often require the application of optional measure-

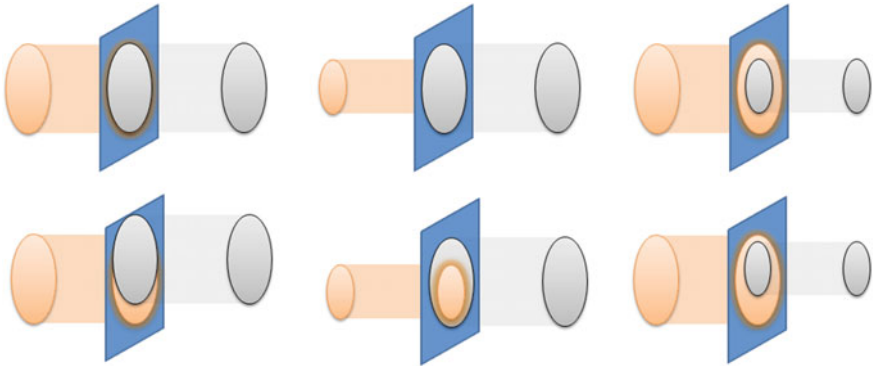

Fig. 8.3 Possible illumination configurations for optimal aligned (top) and slightly misaligned set-up (bottom); On left: Identical incident light spot and field of view of the detector in shape and size in center: small spot for the illuminated light and a large spot for collimated light; On right: Large spot for the illuminated light and a small spot for collimated light

ment accessories, which have to be mounted into the sample compartment and are usually offered for performing reflection measurements at different angles of incidence. The quantification of their systematic measurement errors requires severe own efforts, while corresponding information as included into the manuals—if ever—is usually not very helpful.

In this connection, it is worth mentioning that in many spectrophotometers, I_E, I_T or I_R cannot be measured as directly as it is indicated in Fig. 7.1. Instead, after having interacted with the sample, the light has to pass a certain sequence of optical components before reaching the intensity detector. Therefore, in measurement practice, T and R are accessible from the following set of standard measurements:

- Measurement of an intensity I_{100}, corresponding to an empty sample compartment, i.e. with no sample in the light path (Baseline or Auto Zero measurement)
- Measurement of I_T or I_R with the sample in the light path (sample measurement)
- Measurement of I_0 with the light path blocked (dark signal measurement).

From these intensity data, T and R are obtained in terms of (8.12) [4]:

$$T = \frac{I_T - I_0}{I_{100} - I_0};\ R = \frac{I_R - I_0}{I_{100} - I_0} \tag{8.12}$$

In the case of transmittance measurement at (near) normal incidence, the implementation is straight forward (Fig. 8.4).

In the case that the reflected light has been measured relative to a reference mirror with the reflectance R_{ref}, instead of (8.12), we have:

$$T = \frac{I_T - I_0}{I_{100} - I_0};\ R = R_{ref}\frac{I_R - I_0}{I_{100} - I_0} \tag{8.13}$$

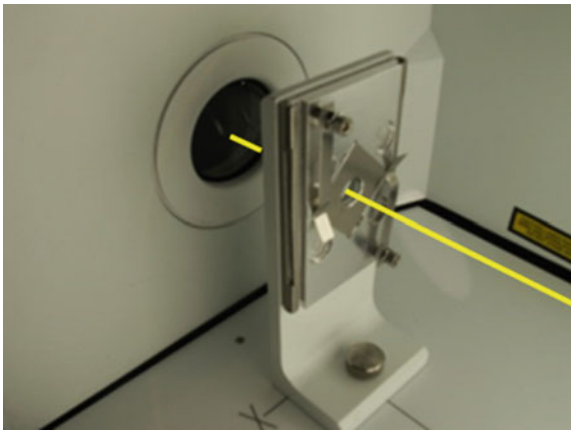

Fig. 8.4 Light path for transmission measurement used in a Perkin Elmer Frontier Optica FTIR

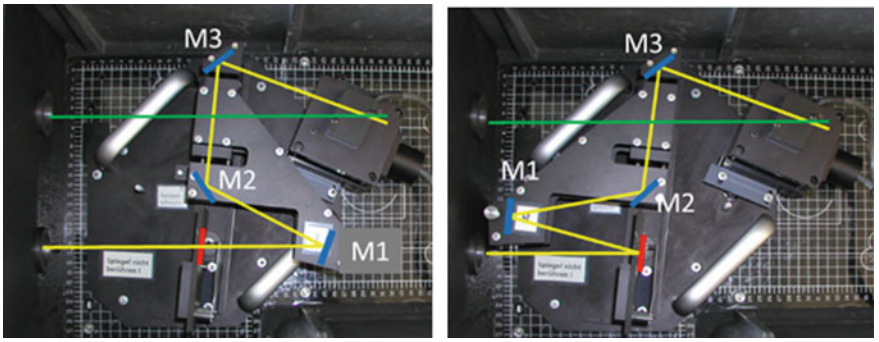

Fig. 8.5 Light path for transmission (left) and reflection measurement (right) in a VN accessory for $\varphi = 6°$

Thereby, normal incidence cannot be realized for geometrical reasons. Reference-free (or absolute) -measurements may be performed by means of special accessories exploiting the so-called VN—measurement principle. The corresponding light path for near normal angle of incidence is shown in Fig. 8.5. It is obvious, that the underlying principle can be easily adapted to oblique incidence. In this case, light polarization as well as effects like beam splitting and displacement must be considered [4].

Basically, two movable mirrors are required to direct the transmitted (Fig. 8.5 left) and reflected light (Fig. 8.5 right). Geometrical constraints may require an additional mirror to direct the light from the sample toward the detector.

A more detailed description is provided in [4] and references cited therein. We also mention here that the VW- and IV-measurement principle s [4] give direct access to R^2 instead of R. They are therefore not suitable for the measurement of very low reflectance values, but strong in the measurement of high reflectances.

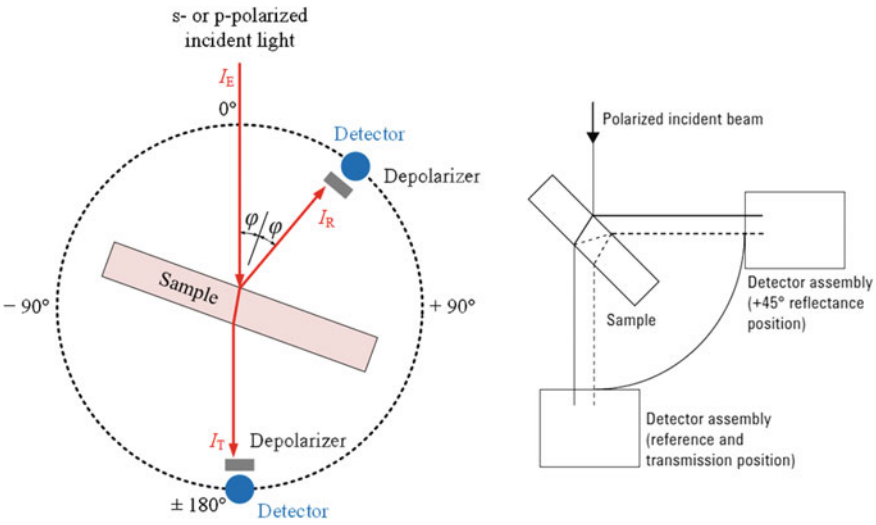

Fig. 8.6 On left: Schematic of the Cary 7000 UMS. Light incident onto the sample can be s- or p-polarized [2]. Absolute specular reflection or transmission can be measured. The detector module allows mounting of an optional depolarizer immediately in front of the detector; On right: Schematic of the Agilent UMA, an absolute variable angle reflectance and transmission accessory, in 45° measurement geometry. Pictures are adapted from [5, 6], and are printed with kind permission by Agilent Technologies Deutschland GmbH

Recently, the Agilent company has developed a measurement system which is adapted to the direct measurement of I_E, I_T or I_R by combining the typical spectrophotometer construction principle with a fully automated mini-goniometer set-up (Cary 7000UMS—compare Fig. 8.6 [5, 6]). It is mounted into an extra sample compartment (the Agilent UMA—Universal Measurement Accessory). The movable detector allows performing direct (reference-free) I_T or I_R measurements at practically any reasonable angle of incidence (Fig. 8.6, on left—compare with Fig. 7.1). The broad detector area even allows collecting the multiply internally reflected light trains which broaden the light beam in oblique incidence conditions (Fig. 8.6, on right, compare also [4]). The recently published TRACK-method for optical thin film characterization [7] is based on the measurement possibilities offered by this innovative spectrometer construction principle.

8.1.4 Pre-processing of Spectra

In principle, measured spectra could be directly used for characterization and any pre-processing of them is not necessarily required. Nevertheless, it may be useful to eliminate superfluous data from measurements.

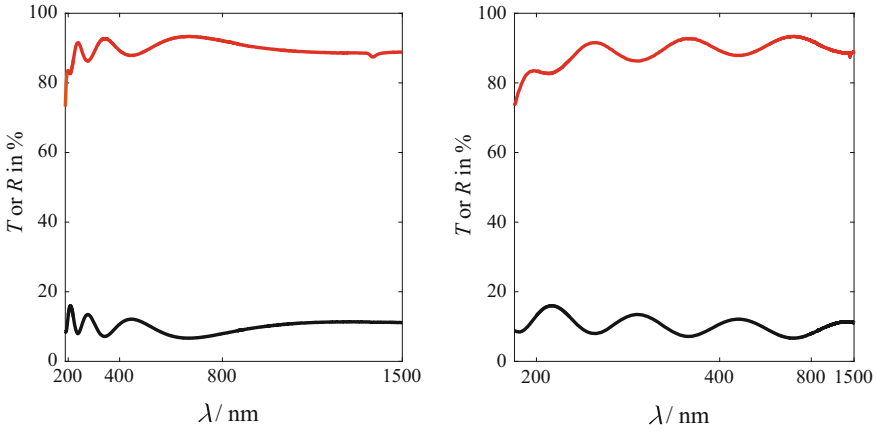

Fig. 8.7 Transmittance and reflectance of an alumina single layer on a fused silica substrate using a wavelength (left) and wavenumber grid (right)

In general, experimental spectra will contain a certain level of random noise. It could be either reduced by averaging multiple measurements on the same sample or by applying some filter to the measured data. It is obvious, that the first approach does not require any a priori knowledge on the spectral characteristic. In the case of normally distributed noise, the noise level for N repeated measurements $\Delta y\,(N)$, each individual measurement with a noise level $\Delta y\,(1)$, can be estimated by

$$\Delta y\,(N) = \frac{\Delta y\,(1)}{\sqrt{N}} \tag{8.14}$$

Therefore, a substantial noise reduction by averaging will commonly result in a significant increase of measurement duration and applying a filter to the measurement data could be prospective. Clearly, the underlying parameters and the algorithm must be carefully selected to minimize resulting systematic errors. Thereby, any a priori knowledge of the spectral characteristic could be very helpful. Common filters used in spectroscopy are Fourier filters and Savitzky-Golay filters [8]. Both filter types can preserve the major features in the spectra and do not affect the grid of the measurement data.

The spatial response of gratings used in dispersive spectrophotometers favors an equidistant wavelength grid for measurements. In the case of single layer coatings on a substrate, this grid will destroy the quasi-periodicity of the interference pattern as shown in Fig. 8.7 on left. Therefore, using an equidistant wavelength grid does not seem to be an efficient choice for coating characterization.

This is not astonishing, because (8.3) will favor a reciprocal stretching of the axes. This could be achieved, when spectra plotted in an equidistant wavenumber grid instead. In this case, the interference pattern appears nearly periodic (Fig. 8.7

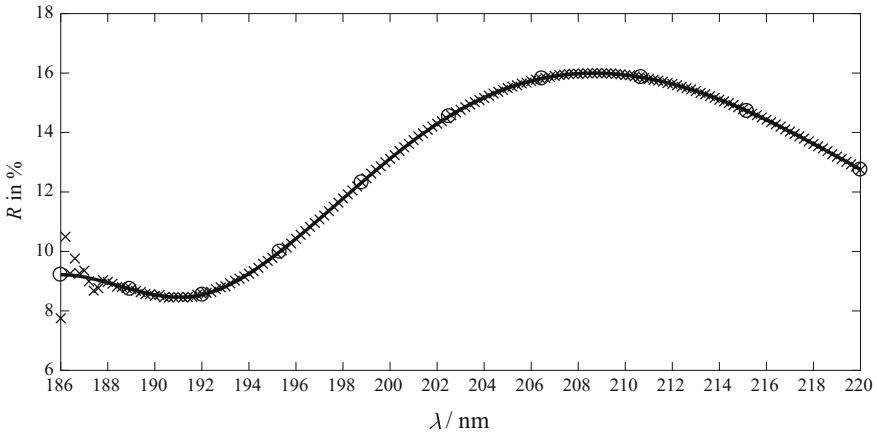

Fig. 8.8 Measured (cross)and pre-processed transmittance spectra (solid line, circles indicate grid) of an alumina single layer on fused silica substrate measured with the 6° VN accessory in the DUV

right). For this reason, an equidistant wavenumber grid appears as the better choice for coating characterization.

Furthermore, a data grid different to the measurement grid may also be useful to eliminate redundant data and to accelerate the characterization process. For this reason, an optional adaption of the data grid during filtering should be considered.

In Fig. 8.8 measured and pre-processed transmittance data of an alumina single layer deposited on a fused silica substrate in the deep ultraviolet (DUV) spectral range is shown. Here, a cubic spline interpolation was used for pre-processing transmittance data. Instead of the huge number of measurement data (crosses), much less data (circles) are used for characterization purposes. Nevertheless, the few wavenumber points (circles) considered for spectra fitting contain all relevant information about the interference pattern.

8.1.5 Specifics of In Situ Spectrophotometry

Photometric measurements in the deposition chamber have already been reported in the previous millennium [9–14]. A overview of the state of the art on optical monitoring techniques can be found at [15]. In this section, we will address only some selected aspects on optical monitoring. Thereby, the broadband monitoring system (OptiMon) developed at the Fraunhofer IOF will be used as an example for a possible implementation. For optical coatings, it clearly will be an advantage to have these measurements available for process control. In contrast to conventional thickness monitoring techniques (e.g. quartz crystal), which only control non-optical properties (e.g. mass), photometric measurements grant access to optical properties of

the layer, and particularly to their optical thickness. Significant progress in sensitivity of detectors, miniaturization and degree of integration of electronic circuits used for sensors, as well as decreasing costs of components and increasing processing speed of computers have led to the result that nowadays photometric measurements are widely used in commercial deposition plants for deposition process control. A large variety of monitoring systems are known and can be classified with respect to spectral range, measurement object, termination criteria and error compensation strategy.

8.1.5.1 Classification of In Situ Monitoring Systems by Spectral Range

The accessible spectral range of a monitoring system is limited by the light source and the spectrometer. Commonly, the complete visible spectral range and parts of the ultraviolet and near infrared spectral regions are covered. *In situ* monitoring systems with broader spectral range are not very common and significantly more expensive.

In general, available solutions can be subdivided into single wavelength and broadband monitoring systems. In single wavelength monitoring systems, transmittance and/or reflectance are either measured at a fixed or variable single wavelength (the latter version is also called *monochromatic* monitoring). Single or monochromatic monitoring systems are known to be very sensitive to random measurement errors [3, 16, 17]. To improve the signal-to-noise ratio, commonly log-in amplifiers are used. In the case of a single fixed wavelength, commonly a monochromatic light source (e.g. laser) is used for illumination. Alternatively, a broadband light source and a monochromator are applied. The monochromator can be either located between light source and sample or between sample and detector. In practice, the location of monochromator in front of the detector (as part of the detector) is preferred, because in this case light from other sources (e.g. plasma/ion source, electron beam gun) is damped by the monochromator, so that the resulting signal-to-noise ratio is better.

In a broadband monitoring system, a broadband light source and a polychromator are used. Depending on the selected type of polychromator, the number of parallel measured wavelength could reach a few thousand. Nowadays, image sensors with up to 250 million pixels for photographic applications are in development [18]. In practice, the useful number of pixels is limited by the optical resolution of the spectrometer, and linear arrays with 2048 pixels are sufficient for most applications. The impact of random noise in a broadband monitoring system is reverse proportional to the square root of (independent) pixels [16]. Therefore, broadband monitoring systems are significantly less sensitive to random noise compared to single wavelength or monochromatic monitoring. Furthermore, broadband monitoring can give access to dispersion of the refractive index. The outlined advantages of broadband monitoring often make it to the preferred approach for new deposition plants.

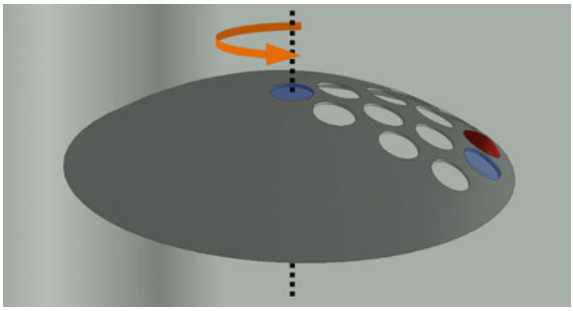

Fig. 8.9 Classification of in situ monitoring systems by measurement object direct monitoring: photometric measurement is performed directly on a relevant sample (red), semi-direct monitoring: photometric measurement is performed on a plane extra substrate (witness glass, blue) located spatially close to the sample, identical performance of the coating on the witness sample and the optical parts is reasonably expected indirect monitoring: photometric measurement is performed on a witness glass (blue) usually mounted at a fixed position in the deposition chamber (e.g. center of the rotating substrate holder), identical performances of the coatings on the witness sample and the optical parts cannot be presumed

8.1.5.2 Classification of In Situ Monitoring Systems by Measurement Object

Depending on the selected measurement object, in situ monitoring approaches are subdivided into *direct*, *semi-direct* and *indirect monitoring* methods [19]—see Fig. 8.9. In the case of *direct monitoring*, the photometric measurement is performed directly on a relevant sample. This approach is commonly preferred for samples with a simple geometry (e.g. plane substrates). In practice, optical parts may have a more complicate geometry (e.g. lenses, prisms) and are not suited for measurements in a generalized measurement configuration. Therefore, a plane extra substrate (the so-called witness sample) is often used for monitoring purposes. In the case of *semi-direct monitoring*, the witness sample is located spatially close to the relevant optical parts, so that an identical performance of the coating on the witness sample and the optical parts is reasonably expected. Direct as well as semi-direct monitoring approaches commonly require a precise synchronization between the movement of the samples and the measurement. The required information could be deducted from different types of sensors. Often, a rotary encoder could be mounted on the driving axes outside the deposition chamber. Alternatively, inductive, capacitive, optical or magnetic sensors inside the plant are used. Moreover, in direct broadband monitoring, the rotating sample holder can be used as a "natural" chopper wheel.

In the case of *indirect monitoring*, the witness glass is usually mounted at a fixed position in the deposition chamber, for example in the center of the rotating substrate holder. Therefore, identical performances of the coatings on the witness sample and the optical parts cannot be expected, so that differences in optical constants, layer thicknesses and further properties must be known. This will cause a serious disadvantage of *indirect monitoring*, because any drift in the assumed behavior will

result in systematic deposition errors and finally limits the achievable accuracy. On the other hand, the use of a fixed witness sample simplifies the design of the measurement system, because synchronization between measurement and movement of the optical parts is no longer required. This will also result in more flexibility on selecting integration time and measurement rate. Additionally, in the case of indirect monitoring, different witness samples can be used during one deposition run, when a witness sample changer is used. Nevertheless, the current trend is towards the application of direct and semi-direct monitoring approaches, because of the superior optical performance.

Further classification of monitoring systems can be performed with respect to deposition termination criteria and deposition error compensation strategies. However, a discussion of these topics will lead us into the field of deposition process optimization and thus beyond the narrower field of optical coating characterization, so that it shall not be performed here. Interested readers are referred to [20].

8.1.5.3 Process Photometer OptiMon

The process photometer OptiMon developed at Fraunhofer IOF (Fig. 8.10) is a broadband monitoring system for industrial deposition plants (e.g. OptoTech OAC-90F, Bühler Syrus pro LCIII). It can be used for direct or semi-direct monitoring and is commonly used to terminate the deposition of homogeneous layers. The halogen light source is located in an MACOR-Ulbricht sphere integrated into the evaporation stop blend and is used to generate a large illuminated spot on the sample, while the collimating optic collects light only from a much smaller sample area, corresponding to the arrangement shown in Fig. 8.3 on right.

This approach provides sufficient tolerance to measure transmittance and relative reflectance of the sample [21], but limits the spectral range to approximately 360—2500 nm. Depending on the used spectrometer, the usable spectral range may

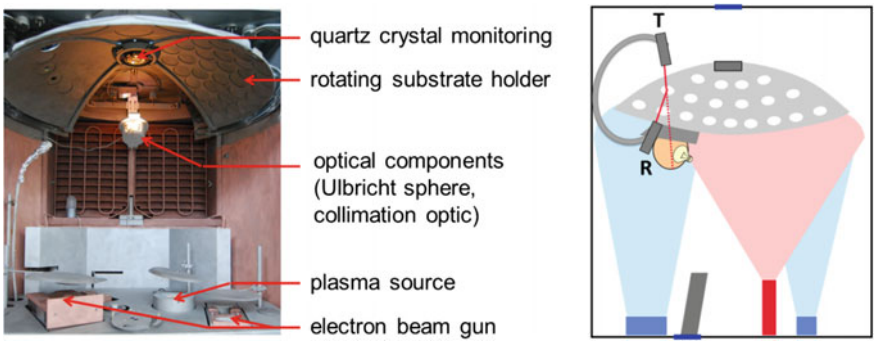

Fig. 8.10 Simultaneous in situ measurement of transmittance and reflectance with process photometer OptiMon in a deposition plant

be further reduced. Currently, two different spectrometers provided by Jeti GmbH [22] are supported:

- PS2000 for wavelength up to 1000 nm
- PS2000 NIR for wavelength in the range 900–1650 nm.

Both devices have built-in hardware for synchronization between sample movement and measurement and internally calculate photometric values from intensity measurements. For determination of layer thicknesses from in situ spectra of homogeneous multilayer systems, a re-engineering software package developed by Alexander Tikhonravov and Michael Trubetskov specifically adapted to the OptiMon system is used. Thereby, the layer thickness during deposition is determined by minimizing (7.17), while breaks between the layer deposition are used to adapt all layer thickness according to (7.18).

Robust re-engineering algorithms use in situ spectra for determining the film thickness assuming that the optical constants are known. They may have been obtained earlier from ex situ measurements performed with suitable single film samples. However, in ex situ conditions, optical constants may be different from those relevant in the vacuum chamber because of atmospheric water which has penetrated into pores in the film. Shift measurements provide a convenient tool to judge differences between ex situ and in situ optical constants. Fortunately, they may be performed by means of the same in situ spectrophotometers.

8.1.6 Shift Measurement

As a further application of in situ spectrophotometry, let us mention measurements of the air-to-vacuum shift of real coatings. In Chap. 2, we have already been in touch with such kind of measurement, when characterizing PIAD zirconia coatings with respect to their porosity. Figure 2.6 shows the change in transmittance of a zirconia film when it is brought from air into vacuum. Once the effective refractive index of a porous coating is dependent on whether the pores are filled with water or not, measurements of the shift give direct access to the porosity of a film, as long as the pores are large enough to exchange water with the surrounding within the measurement time.

In Chap. 2, Sect. 2.3.3e) we have formulated a simple model of a porous layer, which discriminates between rather large and rather small pores, and gives phenomenological access to the water migration kinetics in a porous film. Let y express the full water content in the film, y_l the degree of filling of the large pores, and y_s that of the small pores. The filling or evacuation kinetics of the pores are described in terms of the simple system of differential (2.21):

$$\begin{aligned} p_{\text{''large pores''}} \frac{dy_l}{dt} &= p_{\text{''large pores''}} \kappa_{\perp}(y_0 - y_l) - p_{\text{''small pores''}} \frac{dy_s}{dt} \\ \frac{dy_s}{dt} &= p_{\text{''large pores''}} \kappa_{\text{II}}(y_l - y_s). \end{aligned} \tag{8.15}$$

All symbols have the same meaning as introduced in Sect. 2.3.3e. System (8.15) may be used for calculating the evacuation kinetics as well as the filling kinetics of the pores, dependent on initial conditions and ambient parameter setting.

In order to calculate evacuation kinetics, we shall assume that a sample was held at atmosphere for a time long enough so that all pores are essentially filled with water. Then, at $t = 0$, we assume that it is suddenly brought into vacuum (no water in the ambient). In this case, the following conditions hold:

$$y_0 = 0;\ y_l(t = 0) = 1;\ y_s(t = 0) = 1 \tag{8.16}$$

The full amount of water in the film y is obtained by solving (8.15) and (8.16) according to:

$$\begin{aligned} y(t) &= \frac{p''_{\text{large pores}} f_1 + p''_{\text{small pores}} f_4}{q} e^{-f_3 t} - \frac{p''_{\text{large pores}} f_2 + p''_{\text{small pores}} f_3}{q} e^{-f_4 t} \\ f_1 &= \frac{\kappa_{\text{II}} p - \kappa_\perp + q}{2};\ f_2 = \frac{\kappa_{\text{II}} p - \kappa_\perp - q}{2};\ f_3 = \frac{\kappa_{\text{II}} p + \kappa_\perp - q}{2};\ f_4 = \frac{\kappa_{\text{II}} p + \kappa_\perp + q}{2} \\ q &= \sqrt{\kappa_\perp^2 + 2\kappa_\perp \kappa_{\text{II}} (p''_{\text{small pores}} - p''_{\text{large pores}}) + \kappa_{\text{II}}^2 p^2} \\ p &\equiv p''_{\text{small pores}} + p''_{\text{large pores}} \end{aligned} \tag{8.17}$$

The system of (8.15) also allows calculating the kinetics of water penetration into the pores after film preparation in vacuum conditions. We shall assume now, that at $t = 0$, the pores are initially empty. At $t = 0$, the system is suddenly exposed to (humid) air, so that the ambient parameter y_0 is set equal to 1. Then, instead of (8.16), we now have the conditions (8.18):

$$y_0 = 1;\ y_l(t = 0) = 0;\ y_s(t = 0) = 0 \tag{8.18}$$

The corresponding solution is:

$$\begin{aligned} y(t) &= f_4 (p''_{\text{small pores}} \kappa_{\text{II}} - f_5) \frac{(1 - e^{-f_3 t})}{q \kappa_{\text{II}}} - f_3 (p''_{\text{small pores}} \kappa_{\text{II}} - f_6) \frac{(1 - e^{-f_4 t})}{q \kappa_{\text{II}}} \\ f_5 &= \frac{\kappa_{\text{II}} (p''_{\text{small pores}} - p''_{\text{large pores}}) + \kappa_\perp - q}{2};\ f_6 = \frac{\kappa_{\text{II}} (p''_{\text{small pores}} - p''_{\text{large pores}}) + \kappa_\perp + q}{2} \end{aligned} \tag{8.19}$$

This model calculation results in some important practical conclusions. According to the definition of the shift as given by (2.12), evacuation or venting processes will result in a continuous change in the optical film thickness with time, which is easily accessible by means of in situ spectroscopic tools. Thereby, as it follows from (8.17) and (8.19), that shift may be analytically described as the sum of two different exponential functions with damping constants f_3 and f_4. In practice, their determination may be a straightforward procedure, but their interpretation is not: According to (8.17), f_3 and f_4 are involved functions of the porosity and the exchange rates κ. Nevertheless, in special cases (see Table 8.1), simplified and physically transparent expressions for the dependence of water content on time may be derived:

Table 8.1 Water migration kinetics: Special cases

Condition	Application in practice	Process	Water content in the film
$\kappa_\perp >> \kappa_{II}$	Moderately porous layer	Venting	$y(t) \approx$ $p_{''\text{small pores}''}(1-e^{-p_{''\text{large pores}''}\kappa_{II}t})+$ $p_{''\text{large pores}''}(1-e^{-\kappa_\perp t})$
		evacuation	$y(t) \approx$ $p_{''\text{small pores}''}e^{-p_{''\text{large pores}''}\kappa_{II}t}+$ $p_{''\text{large pores}''}e^{-\kappa_\perp t}$
$\kappa_\perp = \kappa_{II} \equiv \kappa$ $p << 1$	Almost dense layer	Venting	$y(t) \approx$ $p_{''\text{small pores}''}(1-e^{-p_{''\text{large pores}''}\kappa t})+$ $p_{''\text{large pores}''}(1-e^{-\kappa t})$
		evacuation	$y(t) \approx$ $p_{''\text{small pores}''}e^{-p_{''\text{large pores}''}\kappa t}+$ $p_{''\text{large pores}''}e^{-\kappa t}$
$p_{''\text{small pores}''} << p$	Strongly porous layer	Venting	$y(t) \approx p_{''\text{large pores}''}(1-e^{-\kappa_\perp t})$
		evacuation	$y(t) \approx p_{''\text{large pores}''}e^{-\kappa_\perp t}$

Thus, the *moderately porous layers* correspond to the situation sketched earlier in Fig. 2.12. The large pores are in direct correspondence with the ambient, their filling or evacuation kinetics are defined by a time constant dominated by the value of $\kappa_\perp^{-1}$. Small pores, however, have been postulated to exchange water only with the fraction of the large pores. Their filling or evacuation kinetics are therefore dominated by a time constant given by $(p_{''\text{large pores}''}\kappa_{II})^{-1}$. Both time constants are accessible from measurements of the time evolution of the optical film thickness.

In *strongly porous layers* as introduced in Fig. 8.11 the effects caused by filling or evacuation of the large pores are expected to be clearly dominant. The kinetics are practically defined by a simple single exponential function with the time constant $\kappa_\perp^{-1}$.

In *almost dense layers*, however, large open pores are no more expected to be relevant (Fig. 8.11). The introduction of two exchange rates $\kappa_\perp$ and κ_{II} does no more make sense, and the distinction between large and small pores now lacks its formerly obvious geometrical interpretation. According to (8.15), "large pores" merely have to be interpreted as pores which are able to exchange water with other pores *and* the ambient, while "closed pores" do *only* interact with other pores. Within this interpretation, the equations provided in Table 8.1 describe a minor and slow change of the optical thickness with time. In a typical shift measurement, those layers appear to be stable. At longer time scales, as they are typical for storage or aging effects, small gradual changes in the optical behavior may be recorded.

It turns out that shift measurements may give access to qualitative features even of the pore size distribution, although pore diameters are not explicitly present in equations like (2.21) or (8.15). Nevertheless, pore diameters have an implicit impact on the postulated values of the exchange rates as well as the volume fractions of small and large pores. We strongly believe that spectrophotometric shift measure-

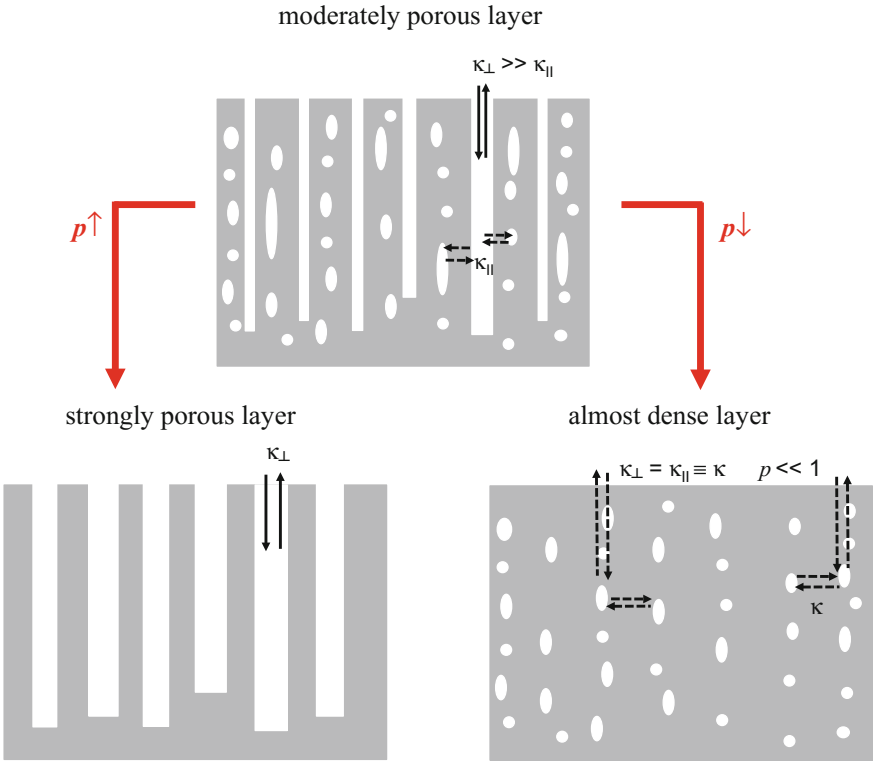

Fig. 8.11 Geometrical visualization of the porosity regimes introduced in Table 8.1. p is here the full porosity

ments do have the potential for determining the pore size distribution in a similar way as it may be done today be means of spectroellipsometric porosimetry [23, 24]. For another alternative approach, see also Sect. 15.2.3 of this book (*Effect of hydrocarbons absorption in thin films at 193 nm*) in this regard.

8.2 Examples

8.2.1 Basics

Classical and often used dispersion models as well as the β_do model [25] have been outlined in Sect. 7.3. For characterization, we will use the wavenumber grid (compare Sect. 8.1.4). In general, a merge of different dispersion models will be used for the following examples.

$$\varepsilon(\nu) = \varepsilon_\infty(\nu) + \chi_{Drude}(\nu) + \chi_{\beta\_do}(\nu) \tag{8.20}$$

Thereby, ε_∞ is the contribution of a single Lorentzian oscillator with assumed negligible line width. In this case, (7.33) simplifies to

$$\varepsilon_\infty(\nu) = 1 + \frac{2J\nu_0}{\pi\left(\nu_0^2 - \nu^2\right)} \tag{8.21}$$

The contribution from the Drude model χ_{Drude} will be modelled by

$$\chi_{Drude}(\nu) = -\frac{\nu_{Drude}^2}{\nu^2 + 2\mathrm{i}\Gamma_{Drude}\nu} \tag{8.22}$$

For the β_do model contribution χ_{β_do} will be calculated using (7.39) and (7.40).

8.2.2 *Ex Situ Characterization of Substrates*

Let us start our presentation of examples with the results of the infrared optical characterization of a bare substrate. Figure 8.12 presents transmission and reflection spectra of a 1 mm thick calcium fluoride substrate, as measured with a Perkin Elmer Frontier Optica FTIR spectrophotometer.

First of all, we recognize that the measured spectral range may be subdivided into two sections: a transparency region, where a remarkable transmission signal may be recorded. This transparency range corresponds to wavenumbers higher than approximately 800 cm^{-1}.

In this transparency range, measured transmission and reflection data are available for characterization. Fortunately, for normal incidence, according to Nichelatti [26] equations for transmittance and reflectance of the uncoated substrate may be

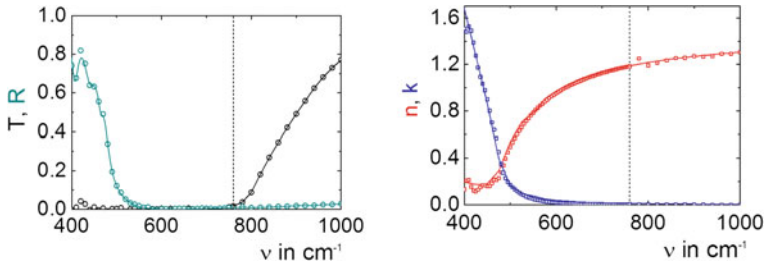

Fig. 8.12 Left: Measure (circle) and modelled (line) transmittance (black) and reflectance (dark cyan) of an uncoated CaF_2 substrate; Right: Calculated (squares) and literature data [27] (line) of the refractive index (red) and extinction coefficient (blue) dashed line marks wavenumber limit used for explicit solution (right) and fit (left)

inverted analytically, so that the calculation of n_{sub} and k_{sub} appears to be a rather straightforward task.

At lower wavenumbers, the transmission is suppressed, so that it is the reflectance only that gives us access to the optical constants. Here, we can make use of a Lorentzian multioscillator model (7.33) to fit the measured reflectance by minimizing a discrepancy function corresponding to the second term in (7.15).

The thus obtained optical constants are presented in Fig. 8.12 on the right together with literature data [27]. The excellent agreement with the literature data confirms us about the consistency of the presented approach.

8.2.3 Ex Situ Characterization of Single Layer Coatings

8.2.3.1 Dielectric Coatings

Here, we present characterization examples for single layer coatings built from hafnia and zirconia. In the transparency region of the corresponding coating, the application of the Lorentzian multi-oscillator model is known to work fine [28]. The task becomes a little bit more challenging, when the fundamental absorption edge is included into the characterization. Commonly, the number of Lorentzian oscillators must be increased. In the case of the hafnia layer, a set of at least 10 Lorentzian oscillators would be required. Thereby, two oscillators have a zero linewidth and only affect the refractive index. Nevertheless, already 28 parameters are used for modelling the dispersion of the optical constants. Therefore, the application of the β_do model (Sect. 7.3.4) seems promising. In fact, a merger of the β_do model (5 parameters with $\alpha = \beta$, $N = 1000$) and (8.21) is required to achieve a practically identical result (Fig. 8.13). This results in a total of only 7 fitting parameters. Thereby, the calculated optical constants show a similar spectral dependence as probably higher densified hafnia layers characterized by the universal dispersion model (Chap. 3 and [29], asterisks). Results from [30] (circles) look also similar, but seem to underestimate refractive index dispersion in the ultraviolet spectral range.

Next, the β_do model is applied to a zirconia single layer coating deposited on fused silica. Here, the coating is opaque for wavenumbers above approximately 47000 cm^{-1} (Fig. 8.14). Nevertheless, spectra could be fitted again using a merger of the β_do model and (8.21). The determined optical constants are in good agreement with data available from [30] (Table 8.2).

8.2.3.2 Semiconductor Coating

The characterization of amorphous germanium (a-Ge) in the UV/VIS/NIR/MIR spectral range using a merger of (8.21), (8.22) and (7.33) appears to be quite challenging a task [31]. Here, considering measurements from the same coating at different φ, on different substrates and coatings with different layer thickness has been required to

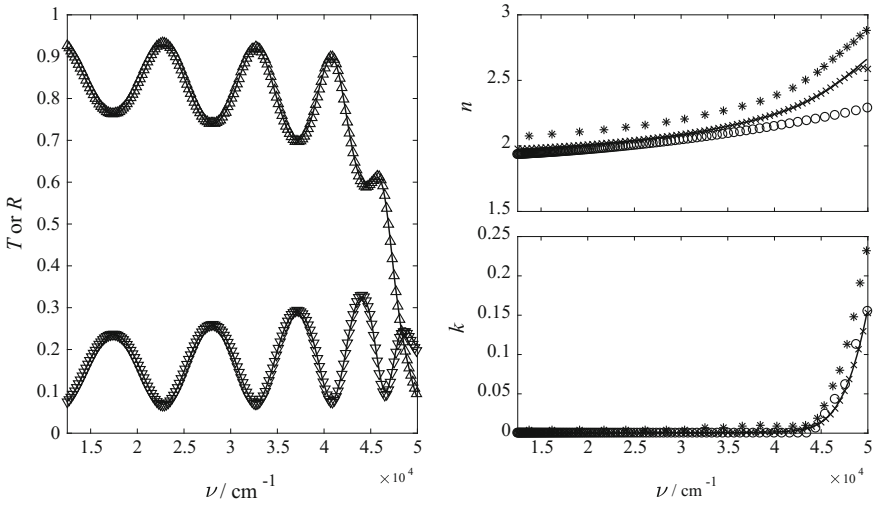

Fig. 8.13 Left: Measured transmittance (upward triangle) and reflectance (downward triangle) and corresponding modelled spectra (solid line) of a hafnia single layer coating on fused silica substrate; Right, Top: Refractive index of hafnia calculated with the β_do model (solid line) and multi-oscillator model (cross) in comparison with published data ([29] asterisks, [30] circles); Right, Bottom: Extinction coefficient calculated with the new model (solid line) and multi-oscillator model (cross)

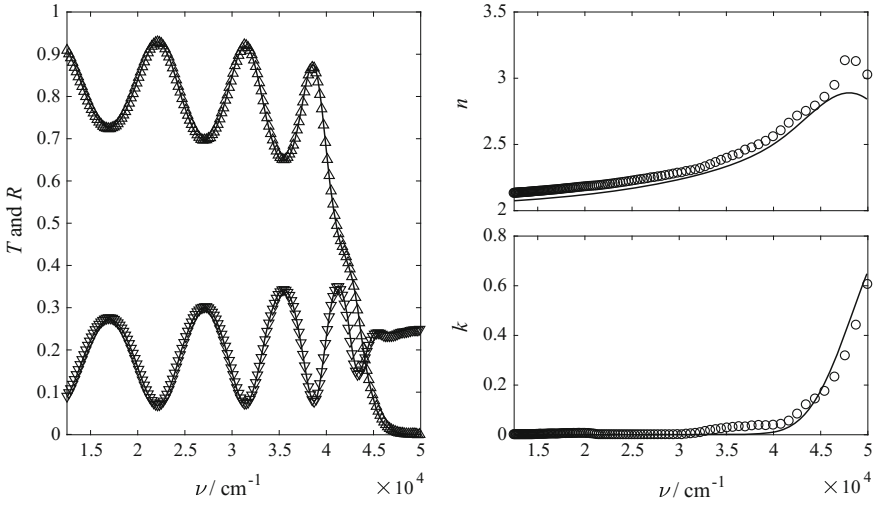

Fig. 8.14 Left: Measured transmittance (downward triangle) and reflectance (upward triangle) and corresponding modelled spectra (solid line) of a zirconia single layer coating on fused silica substrate; Right: Calculated refractive index (solid line, left axes) and extinction coefficient (dotted line, right axes) of zirconia

extract approximately 300 parameters for the multi-oscillator model. It is obvious, that application of the β_do model instead of (7.33) could significantly reduce the number of required parameters and improve the stability of the fitting process. Here, only experimental data from an approximately 100 nm single layer coating on a CaF_2 substrate have been included into the discrepancy function. Transmittance and reflectance spectra measured with the Perkin Elmer Frontier Optica FTIR at near normal incidence and with the 6° and 60° VN-accessory for the Perkin Elmer Lambda 900 are used (Fig. 8.15) for characterization. The calculated optical constants (underlying model parameters are summarized in Table 8.3) are quite smooth and in good agreement with previously published data obtained from the multi-oscillator model [31]. The calculated layer thickness is 102.1 nm and close to expected value. A total of 9 fitting parameters summarized in Table 8.3 is used.

Table 8.2 Model parameters for optical constants of hafnia and zirconia

	$\chi_{\beta\_do}(\nu)$					$\varepsilon_\infty(\nu)$	
	$\nu_{min,1}$ in cm^{-1}	$\nu_{max,1}$ in cm^{-1}	$J_{beta,1}$ in cm^{-1}	$\Gamma_{beta,1}$ in cm^{-1}	$\alpha = \beta$	ν_0 in cm^{-1}	J in cm^{-1}
hafnia	19170	98695	60095	96.3	35.9	87857	300119
zirconia	30253	74582	47423	97.2	13.7	74826	307380

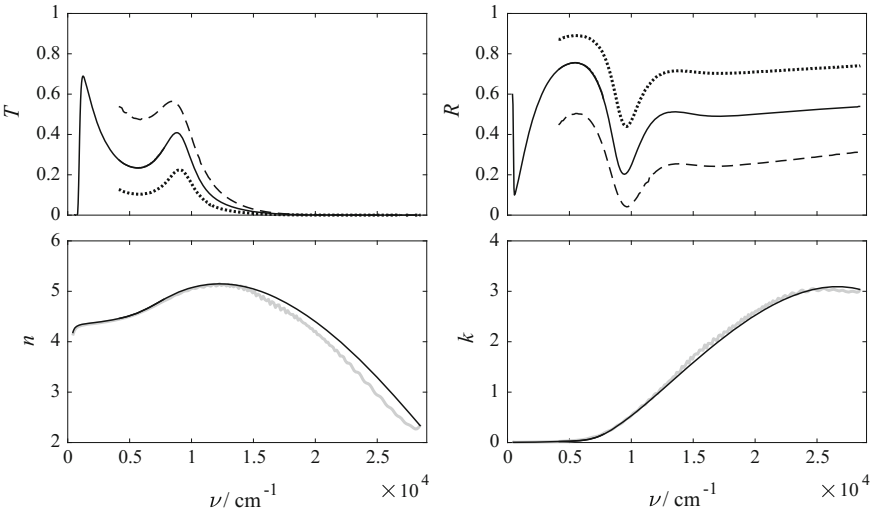

Fig. 8.15 Top: measured transmittance (left) and reflectance (right) of an approximately 100 nm thick a-Ge layer on a CaF_2 substrate measured at near normal incidence in a Frontier Optica FTIR and Lambda 900 equipped with a 6° VN accessory (solid line) and at 60° for s-(dotted line) and p-polarization (dashed) measured in a Lambda 900 equipped with a 60° VN accessory Bottom: Calculated refractive index (left) and extinction coefficient (right) using a merger of a single Lorentzian oscillator with zero linewidth, Drude model and multi-oscillator model (gray line) and β_do model (black line)

Table 8.3 Model parameters for optical constants of a-Ge

$\chi_{Drude}(\nu)$		$\chi_{\beta\_do}(\nu)$					$\varepsilon_\infty(\nu)$	
ν_{Drude} in cm^{-1}	Γ_{Drude} in cm^{-1}	$\nu_{min,1}$ in cm^{-1}	$\nu_{max,1}$ in cm^{-1}	$J_{beta,1}$ in cm^{-1}	$\Gamma_{beta,1}$ in cm^{-1}	$\alpha = \beta$	ν_0 in cm^{-1}	J in cm^{-1}
511.5	5.15	6329.7	36176	388443	376.1	2.79	63703	532173

Table 8.4 Model parameters for optical constants of Cu single layer

$\chi_{Drude}(\nu)$		$\chi_{\beta\_do}(\nu)$					$\varepsilon_\infty(\nu)$	
ν_{Drude} in cm^{-1}	Γ_{Drude} in cm^{-1}	$\nu_{min,1}$ in cm^{-1}	$\nu_{max,1}$ in cm^{-1}	$J_{beta,1}$ in cm^{-1}	$\Gamma_{beta,1}$ in cm^{-1}	$\alpha - 1$	ν_0 in cm^{-1}	J in cm^{-1}
69368	307.6	17711	41413	127101	530.0	2.1e-07	38777	68360

8.2.3.3 Metal Coating

The fit of metal thin film spectra is another difficult task, because the transmittance spectra are suppressed in broad spectral regions, and no interference pattern is observed that could give us valuable a priori information according to what has been discussed in Sect. 7.2.2.2. Nevertheless, reliable spectra fits are possible in terms of a merger (8.21), (8.22) and (7.33), as earlier demonstrated in [2, 32]. Again, we now replace the multioscillator model (7.33) by the β_do model. Underlying model parameters are summarized in Table 8.4. Here, the parameters $\alpha = \beta$ are close to 1 and therefore, the set of oscillators is nearly uniformly distributed.

In Fig. 8.16 we see the spectra fits of an approximately 120 nm thick copper film on fused silica (top). The corresponding optical constants resemble what has been presented in Table 7.2, and we recognize the expected high extinction coefficients ($k \gg n$) in broad spectral regions. The drop in the reflectance around a wavenumber of 20000 cm^{-1} (corresponding to a wavelength of 500 nm) is responsible for the typical color of clean copper surfaces.

Let us denote, that the calculated thickness could be estimated only from the weak transmittance signal around the wavenumber 20000 cm^{-1}. Nevertheless, the calculated layer thickness of 129 nm is close to the expected value.

The underlying model parameters are summarized in Table 8.4. According to the theoretical considerations discussed in Sect. 7.3.1, the parameters of the Drude function shall give information about the plasma frequency ω_p and damping constant of the corresponding metal. In order to provide an impression, Table 8.5 presents corresponding values obtained from the fit compared to literature data.

Note that the thin film relaxation times are generally lower than the reported bulk values; this is a physically consistent result, because real films produced by technologically relevant deposition techniques contain plenty of defects, which give rise to the lower relaxation times for free electrons motion.

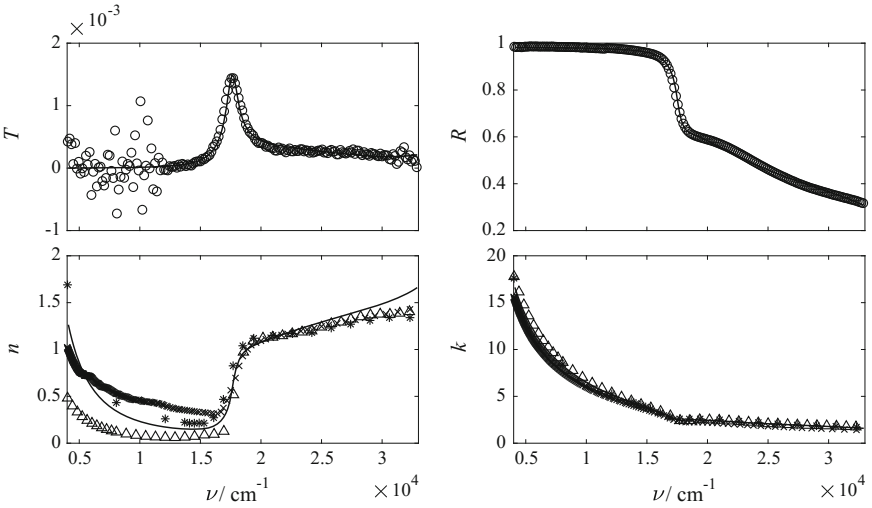

Fig. 8.16 Left: Measured (circle) and modelled (solid line) transmittance and reflectance of an approximately 130 nm thick Cu layer on a fused silica substrate; Right: Modelled refractive index and extinction coefficient (solid line) and literature data (asterisk: [33], triangle [34], cross [35])

Table 8.5 Drude function parameters as obtained from the fit of the Cu film spectra

Model	Estimated plasmon energy		Estimated relaxation time	
	Our fit (single film)	Literature data	Our fit (single film)	Literature data
β_do	8.6 eV	9.3 eV (bulk) [36]	8.6 fs	16-35 fs (bulk) [36]
Lorentzian	9.1 eV		9.7 fs	

8.2.3.4 Organic Dye Coating

Finally, we want to apply the new model to so-called Q absorption band of an approximately 20 nm thick free base phthalocyanine (H_2Pc, Fig. 8.17 [37]) layer deposited on a fused silica substrate. Corresponding transmission and reflection spectra are shown in (Fig. 8.17 left). For this material, application of the multioscillator model to this spectral range is known to be problematic because inhomogeneous broadening of the lines should be considered [38] so that the Brendel model (Table 7.3) may be used instead [39, 40].

When using the β_do model, we have to consider contributions to the optical constants which arise from absorptions outside of the Q-band. To do this, an extended version of (8.21) is used:

$$\varepsilon_\infty(\nu) = 1 + \frac{J_3}{\pi}\left(\frac{1}{\nu_{03} - \nu - \mathrm{i}\Gamma_3} + \frac{1}{\nu_{03} + \nu + \mathrm{i}\Gamma_3}\right) + \frac{2J_4\nu_{04}}{\pi\left(\nu_{04}^2 - \nu^2\right)} \tag{8.23}$$

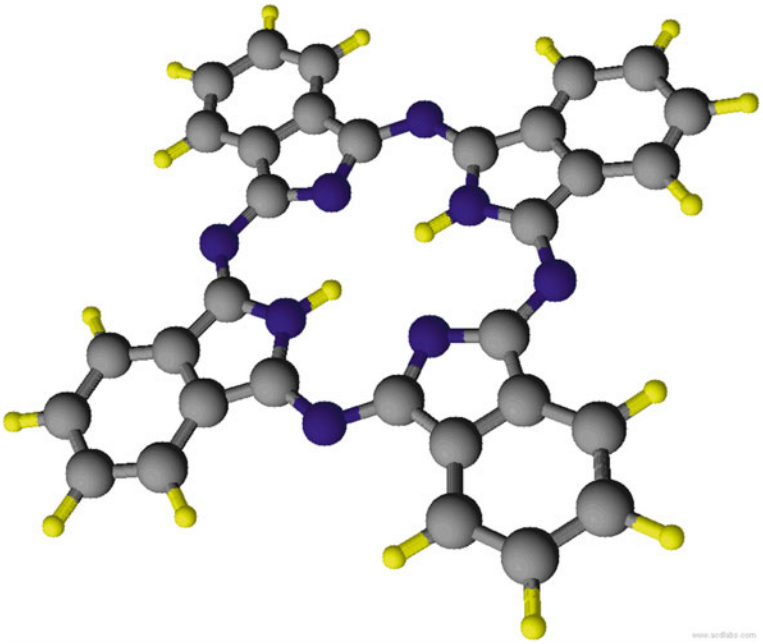

Fig. 8.17 Structure of the H_2Pc molecule calculated with [37]. Hydrogen atoms are shown in yellow, carbon in grey, and nitrogen in navy. Printed with permission of Advanced Chemistry Development, Inc

Table 8.6 Model parameters for optical constants of the H_2Pc single layer

	β_do model				
j	$\nu_{min,j}$ in cm^{-1}	$\nu_{max,j}$ in cm^{-1}	$J_{beta,j}$ in cm^{-1}	$\Gamma_{beta,j}$ in cm^{-1}	$\alpha_j = \beta_j$
1	12907	15110	474.1	2.75	3.60
2	1003.9	30056	7189	369.3	85.5
	Lorentzian oscillators				
	ν_{0j} in cm^{-1}		J_j in cm^{-1}	Γ_j in cm^{-1}	
3	24031		1245.8	1473.0	
4	42754		93302	0	

The calculated model parameters are summarized in Table 8.6 (Fig. 8.18).

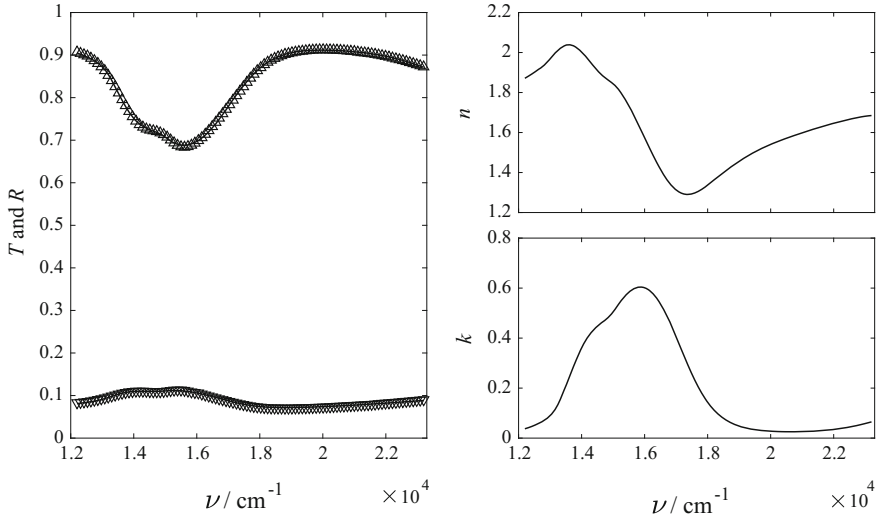

Fig. 8.18 Left: Modelled (line) and measured transmittance (up triangle) and reflectance (down triangle) of an approximately 20 nm thick H_2PC layer on a fused silica substrate; Right: Modelled refractive index (top) and extinction coefficient (bottom)

8.2.4 Interplay of Ex Situ and In Situ Spectroscopy: Preparation and Characterization of a V-Coating

The increased number of parameters and the multiplicity of mathematical solutions make the characterization of multilayer coatings to a quite challenging task. The latter may be addressed by including additional measurement data into the characterization process. Thereby, including of recorded in situ measurement data seems prospective, but may result in further complications when optical constants depends on environment conditions (compare Sect. 8.1.6). Here, some basic concepts will be applied to one of the simplest multilayer coating: a two-layer antireflection coating for 1030 nm at 31° angle of incidence ("V-coating") with a high laser induced damage threshold (LIDT) in the femtosecond regime. In this case, high band gap materials are prospective [41] so that alumina has been selected as high index material and aluminum fluoride as low index material. It is well known, that fluoride coatings are not well-suited for preparation under conditions of ion assistance and therefore, electron beam evaporation without assistance was used for this layer. The resulting porous structure of the coating results in a significant air-to-vacuum shift (Fig. 8.19), which has to be taken into account. The corresponding refractive indices of the AlF_3 film as modelled in terms of (8.21) are shown in Fig. 8.20.

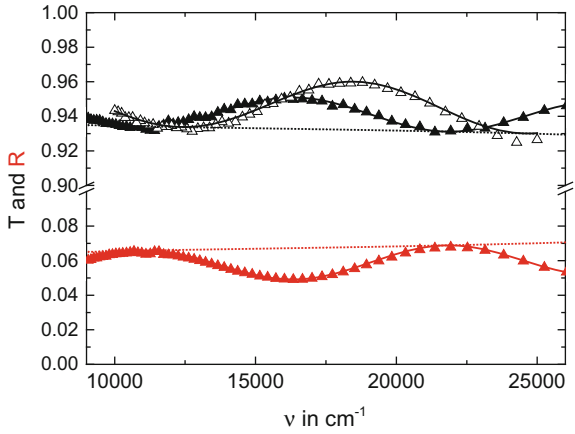

Fig. 8.19 Modelled (solid line) and measured in situ (hollow triangle) and ex situ (filled triangle) transmittance (black) and reflectance (red) of an aluminum fluoride single layer deposited on fused silica (transmittance and reflectance of the uncoated substrate: dotted line)

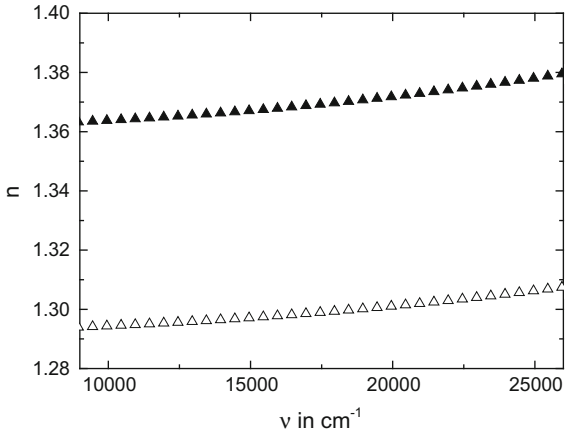

Fig. 8.20 Modelled in situ (hollow triangle) and ex situ (filled triangle) refractive index of an approximately 334 nm thick AlF_3 layer deposited on fused silica

In the case of alumina deposition, two different approaches have been considered:

1. weak assistance and moderate heating during deposition (used later in the design AR1)
2. neither assistance nor heating (used later in the design AR2).

In both cases, ex situ and in situ optical constants have been determined. The corresponding designs AR1 and AR2 for the V-coating (Fig. 8.21) are nearly identical.

For both coatings, the in situ measured transmittance has been in a good agreement with the theoretical performance. In contrast, the ex situ reflectance of AR2 shows significant deviations from the theoretical performance (Fig. 8.22 on right).

Obviously, the assumed optical constants of the AlF_3 layer are not correct when it is deposited on non-assisted alumina (AR2). This may be explained by a different

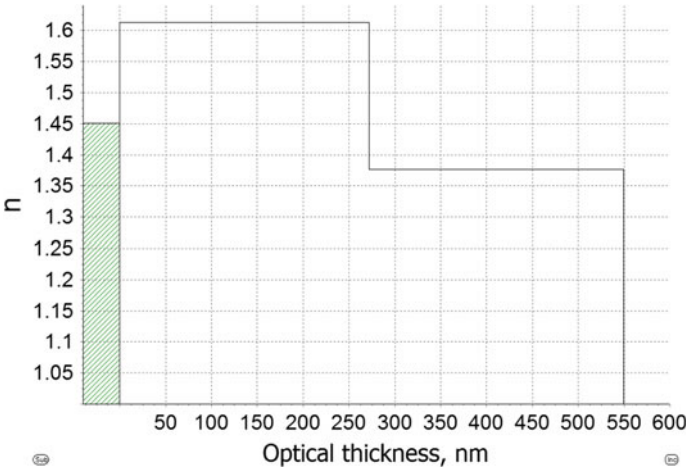

Fig. 8.21 Refractive index profile of the V-coating with weak assistance (AR1: 167.88 nm Al_2O_3, 201.66 nm AlF_3) and no assistance (AR2: 167.55 nm Al_2O_3, 201.70 nm AlF_3)

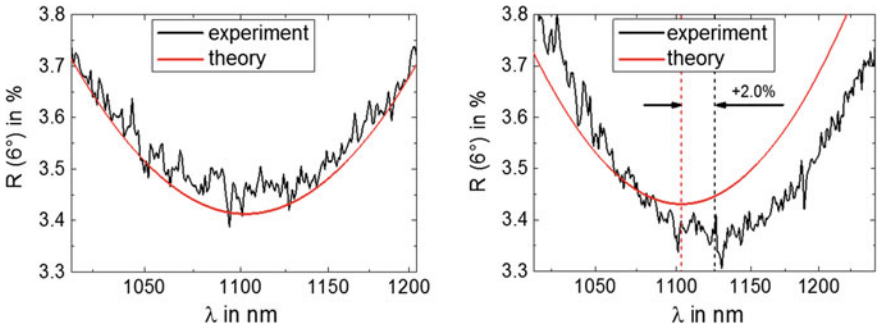

Fig. 8.22 Left: Measured and calculated reflectance of the V coating AR1; Right: Measured and calculated reflectance of the V coating AR2

fluoride growth on a slightly porous alumina layer when being compared with the growth on a fused silica substrate. On porous alumina, the porosity of the resulting fluoride layer also seems to be increased which results in a slightly decreased in situ refractive index, which in turn leads to an increased geometrical thickness when the layer growth is monitored by optical means. That increased thickness explains the observed difference in the minima positions of ex situ measured and calculated reflectance (Fig. 8.22 on right).

Furthermore, the measured LIDT for both the coatings obtained from a series of 429 fs pulses at 1030 nm depends on deposition conditions (Fig. 8.23). The LIDT is 1.89 J/cm^2 for AR1 and 1.32 J/cm^2 for AR2 [42]. Therefore, the weak assistance applied for alumina preparation in AR1 does not only result in a better agreement

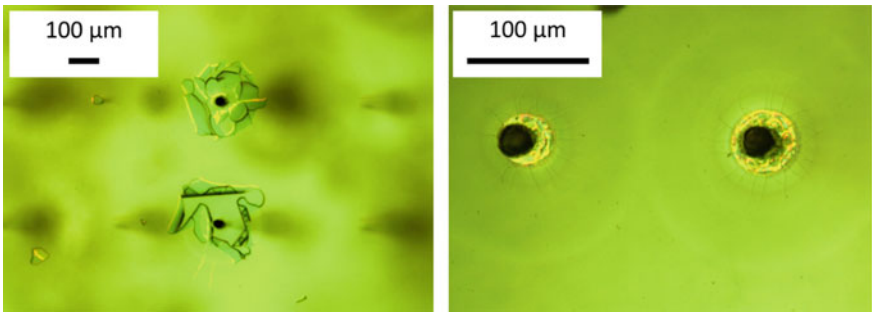

Fig. 8.23 Damage of V-coating AR1 (left) and AR2 (right) after a series of 429 fs pulses at 1030 nm

between experimental and theoretical performances, but also in an improved sub-picosecond LIDT of the coating.

8.3 Conclusions

In this chapter, combined with Chaps. 2 and 7, we have demonstrated the application of spectrophotometric approaches to the characterization of single thin films and a multilayer system. We have presented selected experimental aspects and numerous examples from coating characterization practice. Emphasis was placed on ex situ characterization of single films based on normal incidence transmission and reflection data, which are widely available in practice. For completeness, a more advanced example concerned the inclusion of in situ transmission spectra as well as ex situ data into the characterization strategy for multilayer coatings.

We would like to summarize our analysis in terms of the following theses:

- Spectrophotometry allows determination of the optical constants of thick substrates as well as thin films. This has been demonstrated for selected dielectric, metal and semiconductor films, including an organic dye layer.
- Additionally, spectrophotometry gives access to geometrical construction parameters like the film thickness.
- In complicated samples (for example multilayer coatings), the inclusion of oblique incidence spectra and/or in situ spectra obtained during film deposition may be helpful for enhancing the reliability of the characterization results.
- The obtained optical constants give further access to related quantities, including density, porosity, but also charge carrier density, band structure and possible impurities of the coating. The latter may again be related to results of non-optical characterization techniques like electron microscopy, X-ray-reflection, stoichiometry investigations and the like, and thus contribute to the completion of a physical picture on the nature of the samples investigated.

References

1. H. Kuzmany, *Festkörperspektroskopie. Eine Einführung* (Springer, Berlin Heidelberg New York, 1989)
2. O. Stenzel, *The Physics of Thin Film Optical Spectra: An Introduction*. Springer Series in Surface Sciences, vol. 44, 2nd edn. (Springer, Berlin Heidelberg, 2015)
3. A.V. Tikhonravov, M.K. Trubetskov, M.A. Kokarev, T.V. Amotchkina, A. Duparre, E. Quesnel, D. Ristau, S. Günster, Effect of systematic errors in spectral photometric data on the accuracy of determination of optical parameters of dielectric thin films. Appl. Opt. **41**, 2555–2560 (2002)
4. O. Stenzel, *Optical Coatings: "Material Aspects in Theory and Practice"* (Springer, Berlin Heidelberg, 2014)
5. T. Burt, H. ChuanXu, A. Jiang, Performance of compact visual displays—measuring angular reflectance of optically active materials using the Agilent Cary 7000 Universal Measurement Spectrophotometer (UMS), Agilent Application Note 5991-2508EN, 2013
6. R. Francis, T. Burt, Optical characterization of thin films using a new Universal Measurement Accessory for the Agilent Cary UV-Vis-NIR spectrophotometers, Agilent Application Note 5991-1356EN, 2013
7. R. Vernhes, L. Martinu, TRACK—A new method for the evaluation of low-level extinction coefficient in optical films. Opt. Expr. **23**, 28501–28521 (2015)
8. A. Savitzky, M.J.E. Golay, Smoothing and differentiation of data by simplified least squares procedures. Anal. Chem. **36**, 1627–1639 (1964)
9. B. Vidal, A. Fornier, E. Pelletier, Optical monitoring of nonquarterwave multilayer filters. Appl. Opt. **17**, 1038–1047 (1978)
10. B. Vidal, A. Fornier, E. Pelletier, Wideband optical monitoring of nonquarterwave multilayer filters. Appl. Opt. **18**, 3851–3856 (1979)
11. P.J. Bruce, I.J. Hodgkinson, A stable optical photometer for vacuum coating. J. Vac. Sci. Technol., A **3**, 436–437 (1985)
12. F.J. van Milligen, H.A. Macleod, Development of an automated scanning monochromator for monitoring thin films. Appl. Opt. **24**, 1799–1802 (1985)
13. I. Powell, J.C.M. Zwinkels, Development of optical monitor for control of thin film deposition. Appl. Opt. **25**, 3645–3652 (1986)
14. R.P. Netterfield, P.J. Martin, K.H. Müller, In-situ optical monitoring of thin film deposition. SPIE **1988**, 10–15 (1012)
15. B.T. Sullivan, G. Carlow, An overview of optical monitoring techniques, in *Optical Interference Coatings, OSA Technical Digest* (Optical Society of America, 2010, paper TuC1
16. A.V. Tikhonravov, M.K. Trubetskov, T.V. Amotchkina, Investigation of the effect of accumulation of thickness errors in optical coating production by broadband optical monitoring. Appl. Opt. **45**, 7026–7034 (2006)
17. A.V. Tikhonravov, M.K. Trubetskov, Elimination of cumulative effect of thickness errors in monochromatic monitoring of optical coating production: theory. Appl. Opt. **46**, 2084–2090 (2007)
18. http://www.canon.com/news/2015/sep07e.html
19. R.R. Willey, *Practical Design and Production of Optical Thin Films*, 2nd edn. (CRC Press, 2002). ISBN 9780824708498
20. A.V. Tikhonravov, M.K. Trubetskov, T.V. Amotchkina, Optical monitoring strategies, in ed. by Piegari, Flory, *Optical Thin Films and Coatings* (Woodhead Publishing Limited, 2013)
21. J. Gäbler, O. Stenzel, S. Wilbrandt, N. Kaiser, Optische in-situ Prozessverfolgung und -steuerung des Aufdampfens optischer Beschichtungen durch gleichzeitige Messungen des Transmissions- und Reflexionsvermögens der wachsenden Schicht. Vak. Forsch. Prax. **25**(6), 22–28 (2013)
22. http://www.jeti.com
23. M.R. Baklanov, K.P. Mogilnikov, V.G. Polovinkin, F.N. Dultsev, Determination of pore size distribution in thin films by ellipsometric porosimetry. J. Vac. Sci. Technol. B, 1385–1391 (2000)

24. C. Murray, C. Flannery, I. Streiter, S.E. Schulz, M.R. Baklanov, K.P. Mogilnikov, C. Himcinschi, M. Friedrich, D.R.T. Zahn, T. Gessner, Comparison of techniques to characterise the density, porosity and elastic modulus of porous low-k SiO xerogel films
25. S. Wilbrandt, O. Stenzel, Empirical extension to the multioscillator model: the beta-distributed oscillator model. Appl. Opt. **56**, 9892-9899 (2017)
26. E. Nichelatti, Complex refractive index of a slab from reflectance and transmittance: analytical solution. J. Opt. A: Pure Appl. Opt. **4**, 400–403 (2002)
27. E.D. Palik (ed.), *Handbook of Optical Constants of Solids,* vol. I, II (Academic Press, Orlando, 1998), pp. 753–763, 766–775, 830–835
28. K. Friedrich, S. Wilbrandt, O. Stenzel, N. Kaiser, K.H. Hoffmann, Computational manufacturing of optical interference coatings: method, simulation results, and comparison with experiment. Appl. Opt. **49**, 3150–3162 (2010)
29. D. Franta, D. Nečas, I. Ohlídal, Universal dispersion model for characterization of optical thin films over a wide spectral range: application to hafnia. Appl. Opt. **54**, 9108–9119 (2015)
30. Center for Nanolithography Research, Rochester Institute of Technology, http://www.rit.edu/~w-lith/thinfilms/thinfilms/thinfilms.html
31. S. Wilbrandt, C. Franke, V. Todorova, O. Stenzel, N. Kaiser, Infrared optical constants determination by advanced FTIR techniques, in *Optical Interference Coatings 2016, OSA Technical Digest* (online) (Optical Society of America, 2016), paper MC.10
32. O. Stenzel, S. Wilbrandt, N. Kaiser, Spektralphotometrische Messungen zur Charakterisierung und Qualitätskontrolle von Oberflächen und Schichten, Colloquium optische Spektrometrie (COSP), 17./18.03.2014
33. H.J. Hagemann, W. Gudat, C. Kunz, Optical constants from the far infrared to the x-ray region: Mg, Al, Cu, Ag, Au, Bi, C, and Al2O3. J. Opt. Soc. Am. **65**, 742–744 (1975)
34. S. Babar, J.H. Weaver, Optical constants of Cu, Ag, and Au revisited. Appl. Opt. **54**, 477–481 (2015)
35. M.R. Querry, Optical constants, Contractor Report CRDC-CR-85034 (1985)
36. H. Ehrenreich, H.R. Philipp, Optical properties of Ag and Cu. Phys. Rev. **128**, 1622–1629 (1962)
37. ACD/ChemSketch (Freeware), version 2016.2, Advanced Chemistry Development, Inc., Toronto, ON, Canada, www.acdlabs.com, 2016
38. The linear optical constants of thin phthalocyanine and fullerite films from the near infrared up to the UV spectral regions: Estimation of electronic oscillator strength values
39. R. Brendel, D. Bormann, An infrared dielectric function model for amorphous solids. J. Appl. Phys. **71**, 1–6 (1992)
40. A. Franke, A. Stendal, O. Stenzel, C. von Borczyskowski, Gaussian quadrature approach to the calculation of the optical constants in the vicinity of inhomogeneously broadened absorption lines. Pure Appl. Opt. **5**, 845–853 (1996)
41. M. Jupe et al., Mixed oxide coatings for advanced fs-laser applications. Proc. SPIE **6720**, 67200U (2007)
42. Final report, Optische Komponenten und Baugruppen mit hohen Lebensdauern für Ultrakurzpuls-Laser und Systeme (Ultra-LIFE), FKZ: 13N11555, Technische Informationsbibliothek